J. Fluid Mech. (2023), *vol*. 977, A10, doi:10.1017/jfm.2023.955

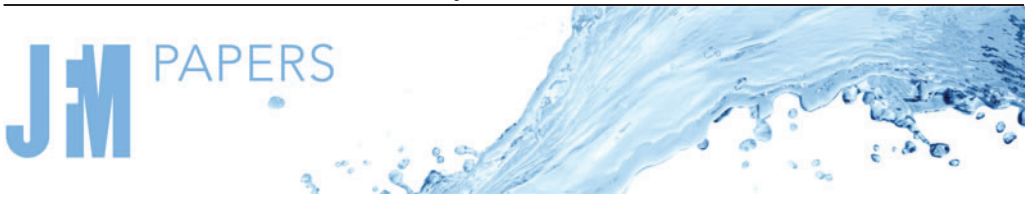

Daughter oil droplet entrainment by oil-coated bubble bursting

Zhengyu Yang[1], **Bingqiang Ji**[1,‡] **and Jie Feng**[1,2,†]

[1]Department of Mechanical Science and Engineering, University of Illinois at Urbana–Champaign, Urbana, IL 61801, USA

[2]Materials Research Laboratory, University of Illinois at Urbana–Champaign, Urbana, IL 61801, USA

(Received 17 May 2023; revised 25 August 2023; accepted 3 November 2023)

Compound bubbles with a liquid coating in another continuous immiscible bulk phase are ubiquitous in a wide range of natural and industrial processes. Their formation, rise and ultimate bursting at the air–liquid interface play crucial roles in the transport and fate of natural organic matter and contaminants. However, the dynamics of compound bubbles has not received considerable attention until recently. Here, inspired by our previous work (Yang *et al.*, *Nat. Phys.*, vol. 19, 2023, pp. 884–890), we investigate the entrainment of daughter oil droplets in bulk water produced by a bursting oil-coated bubble. We document that the size of the entrained daughter oil droplet is affected by the oil coating fraction and the bulk liquid properties. We rationalize this observation by balancing the viscous force exerted by the extensional flow produced by bubble bursting with the capillary force resisting the deformation of the oil coating, and considering the subsequent end-pinching process which finally entrains the daughter oil droplets. We propose a scaling analysis for the daughter oil droplet size that well captures the experimental results for a wide range of oil coating fractions and Ohnesorge numbers of the bulk liquid. In addition, we discuss the non-monotonic variation of daughter droplet size with the Ohnesorge number, and show the eventual absence of daughter droplets because of the strong viscous effect in the high-Ohnesorge-number regime. Our findings may advance the fundamental understanding of compound bubble bursting and provide guidance and modelling constraints for bubble-mediated contaminant transport in liquids.

Key words: breakup/coalescence, bubble dynamics, multiphase flow

1. Introduction

Bubbles present in liquids are commonplace in a wide spectrum of natural and industrial processes. From formation, through motion, until bursting, bubbles inevitably interact

† Email address for correspondence: jiefeng@illinois.edu
‡ Present address: Department of Mechanical Engineering, City University of Hong Kong, Hong Kong 999077, China. Email address for correspondence: bingqiji@cityu.edu.hk.

with the surrounding liquid. As a consequence of the ubiquitous heterogeneity of the liquids in nature and industry, bubbles may collect impurities or pollutants in bulk liquids, finally forming structurally compound bubbles. For instance, rising bubbles in the ocean have been found to capture surface-active materials from the water column (Walls, Bird & Bourouiba 2014) and facilitate the formation of an organic-enriched air–sea interface known as the sea surface microlayer (Tseng *et al.* 1992; Wang *et al.* 2017). Other examples include oil-laden bubbles released from natural seeps in the deep sea (Johansen, Todd & MacDonald 2017), froth flotation with oily bubbles (Su, Xu & Masliyah 2006; Zhou *et al.* 2014) and material processing using compound bubbles (Visser *et al.* 2019; Behrens 2020). In the context of a bursting bubble at a liquid–air interface, most previous studies have focused on the dynamics of clean bubbles (Lhuissier & Villermaux 2012; Deike *et al.* 2018). Only recently has the bursting dynamics of such compound bubbles attracted considerable attention (Ji, Yang & Feng 2021*b*; Yang *et al.* 2023). The structurally compound interface has been shown to profoundly modify the bubble-mediated mass and momentum transport across the interface, and thus requires further investigation.

In particular, our recent work highlights that oil-coated, free-surface bubble bursting enhances aerosol formation and transmission by producing upward jets that are smaller and faster than those formed by pristine bubbles (Yang *et al.* 2023). Bursting of bubbles at liquid surfaces refers to the rupture of the bubble cap film and the following collapse of the bubble cavity. The associated dynamics has remained a canonical research topic in interfacial flows due to its importance in mediating the mass transport across the interface, such as sea spray aerosol generation impacting the climate (Wilson *et al.* 2015), aerosolization of contaminated water for airborne disease transmission (Poulain & Bourouiba 2018) and even vegetative reproduction over natural bodies of water (Hariadi, Winfree & Yurke 2015). Specifically, during cavity collapse, capillary waves are excited and propagate toward the bottom of the bubble cavity. When the capillary waves collide at the bubble cavity bottom, the upward jet is produced (Duchemin *et al.* 2002). The morphology of the upward jet has been extensively studied (Deike 2022), but the dynamics and transport associated with the bulk flow under the bubble cavity have received much less attention.

With the focusing of capillary waves at the bubble cavity nadir, a region characterized as a ‘downward jet’ is produced with downward velocity below the bubble bottom. The flow field in this region was first experimentally characterized by the pioneering work of MacIntyre (1972). Later work further showed that the downward jet region exhibited features of an elongational flow (Garcia-Briones & Chalmers 1994), and it was reported that the high hydrodynamic stress associated with the elongational flow could cause cell damage in biological industry (Boulton-Stone & Blake 1993). Indeed, bubble bursting is one of the main mechanisms for cell death in sparging bioreactors (Walls *et al.* 2017). The energy dissipation rates in the downward jet region during bubble bursting were found to be strong enough to even kill the cells (Boulton-Stone & Blake 1993; Garcia-Briones, Brodkey & Chalmers 1994; Walls *et al.* 2017). In addition, it has been suggested that cells in bioreactors tend to be killed by the presence of small bubbles since both the maximum extensional stress and the energy dissipation rate decrease with the bubble radius (MacIntyre 1972; Boulton-Stone & Blake 1993; Garcia-Briones *et al.* 1994; Tran *et al.* 2016).

Here, we investigate a distinct feature related to the downward jet and bulk extensional flow induced by a bursting oil-coated bubble, regarding the daughter oil droplet entrainment below the bubble cavity. With systematic experiments, we demonstrate that oil-coated bubble bursting results in the breakup of the oil coating into smaller droplets in the bulk aqueous liquid. We further provide a scaling law to correlate

the daughter oil droplet size to the oil coating fraction and the physical properties of the bulk liquid, which captures the experimental results well. This paper is structured as follows. Our experimental set-up is described in § 2. In § 3, we first present the experimental observations for the daughter oil droplet formation in § 3.1, and then show the spatio-temporal evolution of the oil blob in the extensional flow in § 3.2. We further derive the scaling law for the size of the entrained daughter oil droplet by illustrating the mechanism of end pinching in § 3.3, and also provide a discussion of the regime without daughter oil droplet entrainment with a high bulk liquid viscosity in § 3.4. Finally, we summarize the main conclusions in § 4.

2. Experimental methods

The oil-coated bubbles are produced using a custom-designed coaxial orifice system (Ji, Yang & Feng 2021*c*), in a square transparent acrylic container with dimensions of 20 mm × 20 mm × 25 mm. The system consists of a small stainless inner needle with an inner diameter of 0.41 mm, plugged in a stainless outer needle with an outer diameter of 3.43 mm. The bubbles are formed by injecting air through the inner needle to a sessile oil drop formed through the injection of the outer needle, until the oil-coated bubble detaches because of buoyancy. The equilibrium bubble radius R is measured to be 2.1 ± 0.3 mm, consistent with the previous model prediction in our work (Ji *et al.* 2021*c*). By adjusting the volume of the sessile oil drop above the outer needle before air injection, we can control the oil volume fraction of the generated oil-coated bubble (Ji, Singh & Feng 2021*a*). The bubble then rises to the free air–water surface and ultimately bursts. The bursting process is captured by a high-speed camera (Photron Mini AX200) from the bottom-side view, under the illumination of a white LED backlight (Phlox 100 × 100 HSC), and with a frame rate of 6400 frames per second and a magnification of 2–4. The magnification corresponds to a spatial resolution of 5–10 μm pixel^{-1}, which can serve as a reference of the error limits. In all figures, the error bars are smaller than the size of the data points.

Regarding the working liquids, we use glycerine–water mixtures with a glycerine weight fraction $w_g = 0\,\%$–$84.2\,\%$ (corresponding to a viscosity range of $\mu_w = 1.1$–94 mPa s) as the bulk liquid, and silicone oils with viscosity $\mu_o = 0.9$–20 mPa s (Sigma-Aldrich) as the bubble coating liquids. The viscosities of the liquids are measured using a controlled stress rheometer (DHR-3, TA Instrument) with a cone–plate geometry (40.0 mm diameter, cone angle 0.993°, 28 μm truncation), at a controlled temperature of 20 °C. In our experiments, the silicone oils fully engulf the gas bubbles due to the positive spreading coefficient $S = \gamma_{wa} - \gamma_{ow} - \gamma_{oa}$. Here, γ is the interfacial tension, and the subscripts wa, ow and oa represent aqueous solution–air, aqueous solution–oil and oil–air, respectively. The interfacial tensions are measured by pendant drop method with in-house MATLAB codes (Song & Springer 1996). All the liquid properties are listed in table 1. The volume of the oil coating V_o engulfing the bubble is estimated by measuring the volume of the oil blob before jet formation, and the oil volume fraction is calculated as $\psi_o = 3V_o/(4\pi R^3)$. Specifically, we focus on the dynamics of bubbles coated with a thin layer of oil. Thus, the oil fraction ψ_o is controlled between 0.12 % and 10.0 % (spanning two orders of magnitude) with the maximum oil layer thickness less than $0.2R$.

3. Results and discussion

3.1. *Daughter oil droplet entrainment in water*

Figure 1(*a–c*) shows the experimental observation for the entrainment of a daughter oil droplet in the bulk liquid during oil-coated bubble bursting. Here, the origin of time $t = 0$

w_g (%)	ρ_o (kg m^{-3})	ρ_w (kg m^{-3})	μ_o (mPa s)	μ_w (mPa s)	γ_{ow} (mN m^{-1})	γ_{oa} (mN m^{-1})	γ_{wa} (mN m^{-1})
84.2	820	1219	0.9 ± 0.1	94 ± 2	29.7 ± 0.3	13.1 ± 0.4	65.3 ± 0.5
78.2	820	1203	0.9 ± 0.1	47.6 ± 0.4	30.8 ± 0.2	13.1 ± 0.4	67.9 ± 0.5
68.3	820	1179	0.9 ± 0.1	19.4 ± 0.1	33.9 ± 0.3	13.1 ± 0.4	69 ± 1
58.7	820	1150	0.9 ± 0.1	9.5 ± 0.1	29.8 ± 0.2	13.1 ± 0.4	65.5 ± 0.7
46.5	820	1117	0.9 ± 0.1	4.9 ± 0.1	30.7 ± 0.5	13.1 ± 0.4	66.7 ± 0.7
24.2	820	1058	0.9 ± 0.1	2.1 ± 0.1	29.0 ± 0.3	13.1 ± 0.4	69.4 ± 0.7
0	820	998	0.9 ± 0.1	1.1 ± 0.1	27.3 ± 0.3	13.1 ± 0.4	71 ± 1
0	913	998	4.6 ± 0.1	1.1 ± 0.1	38.1 ± 0.4	18.7 ± 0.3	71 ± 1
0	950	998	20.0 ± 0.1	1.1 ± 0.1	40.9 ± 0.5	19.4 ± 0.7	71 ± 1

Table 1. Physical properties of liquids used in the experiments (w_g: weight fraction of glycerine in the aqueous solution; ρ_o: oil density; ρ_w: aqueous solution density; μ_o: oil viscosity; μ_w: aqueous solution viscosity; γ_{ow}: oil–aqueous solution interfacial tension; γ_{oa}: oil–air interfacial tension; γ_{wa}: aqueous solution–air interfacial tension).

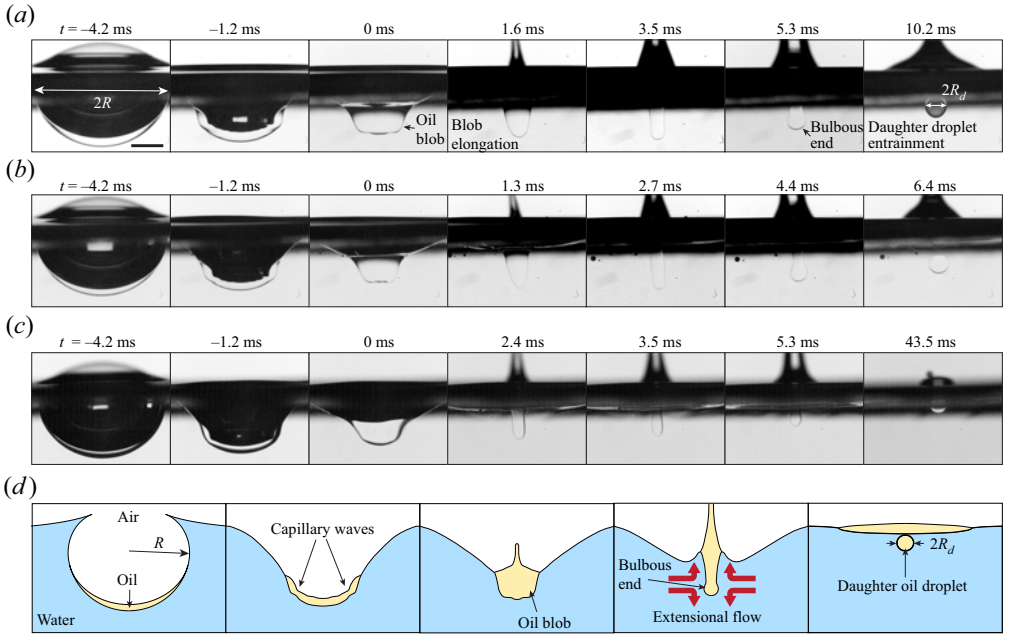

Figure 1. (*a–c*) High-speed images showing the bottom-side view of the daughter oil droplet entrainment during oil-coated bubble bursting, with different bulk liquid viscosity μ_w and oil volume fraction ψ_o: (*a*) $\mu_w = 2.1$ mPa s, $\psi_o = 5.6\,\%$; (*b*) $\mu_w = 2.1$ mPa s, $\psi_o = 4.0\,\%$; and (*c*) $\mu_w = 9.5$ mPa s, $\psi_o = 4.0\,\%$. The oil viscosity is $\mu_o = 0.9$ mPa s for all images. Here, $t = 0$ is defined as the moment when the curvature of the oil–air surface at the bottom pole reverses during cavity collapse. The scale bar represents 1 mm. (*d*) Schematics of daughter oil droplet entrainment by a bursting oil-coated bubble.

is defined as the moment when the curvature of the oil–air surface at the bottom pole reverses during the collapse of the bubble cavity. The cavity collapse starts after the bubble cap ruptures, and capillary waves are excited by the capillary retraction of the liquid film following the cap rupture and propagate along both the air–oil and water–oil interfaces ($t = -1.2$ ms in figure 1*a*). The oil coating is swept by the capillary waves downwards,

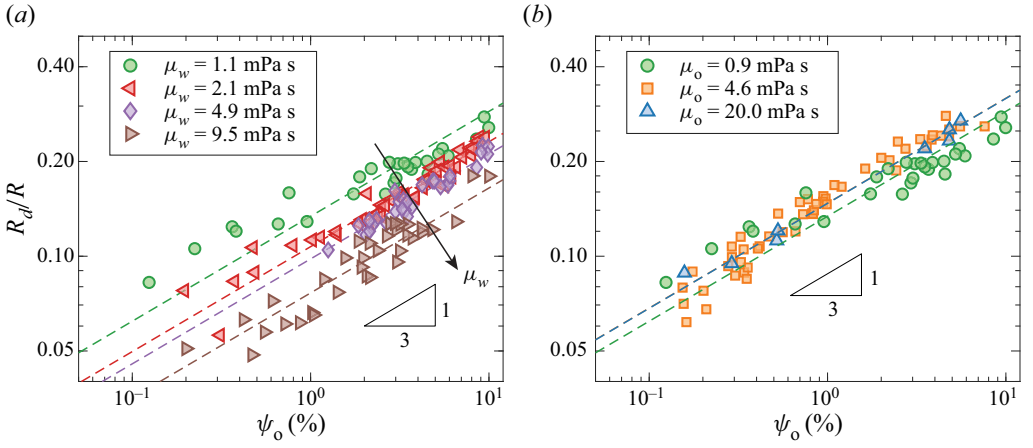

Figure 2. Daughter oil droplet radius scaled with bubble radius, R_d/R, as a function of ψ_o: (*a*) at the same oil viscosity μ_o of 0.9 mPa s and different bulk viscosity μ_w; (*b*) at the same μ_w of 1.1 mPa s and different μ_o. The dashed lines represent the lines of best fit using $R_d/R = C\psi_o^{1/3}$.

forming an oil blob ($t = 0$ ms in figure 1*a*). At the same time, the wave focusing during cavity collapse produces an extensional flow around the cavity nadir. The extensional flow not only produces an upward jet at the oil–air interface, which ejects tiny oil droplets in the air (Yang *et al.* 2023), but also generates a downward jet in the liquid phase (MacIntyre 1972; Boulton-Stone & Blake 1993). The downward jet stretches the oil blob ($t = 0$–3.5 ms in figure 1*a*), where the oil blob elongates and decreases in width until a bulbous end develops at its bottom part ($t = 5.3$ ms in figure 1*a*). The bulbous end moves faster than the oil in the blob located just above it, and thus the oil gets into the bulbous end and inflates it. A neck forms above the bulbous end, and narrows progressively until a daughter oil droplet pinches off ($t = 10.2$ ms in figure 1*a*). These hydrodynamic features, summarized in figure 1(*d*), are similar to the dynamics of deformation and end pinching of a droplet under an extensional flow in previous studies (Stone, Bentley & Leal 1986; Schulkes 1996; Li, Renardy & Renardy 2000; Anthony *et al.* 2019). From the above observations, we consider the daughter oil droplet entrainment as two successive processes, i.e. oil blob elongation under the extensional flow followed by end pinching of the oil bulb. While multiple oil droplets could be observed in some cases, in the current work we only focus on the largest daughter droplet pinching off from the end of the elongated oil blob.

We perform systematic experiments to first investigate the relationship of the daughter oil droplet radius R_d to the oil coating fraction ψ_o and liquid viscosities. As shown in figure 2(*a*), the dimensionless daughter oil droplet radius R_d/R increases with ψ_o at a fixed liquid combination. Meanwhile, for the same ψ_o, R_d decreases dramatically when the bulk viscosity μ_w increases from 1.1 to 9.5 mPa s (figure 2*a*), while it barely changes when the oil viscosity μ_o increases from 0.9 to 20.0 mPa s (figure 2*b*). We demonstrate that the non-dimensionalized droplet radius follows $R_d/R \sim \psi_o^{1/3}$ regarding a wide range of ψ_o (figure 2). This proportionality shows that the droplet size R_d directly scales with the global size of the blob $R_o = R\psi_o^{1/3}$ in the current experiments. The characteristic length scale for the daughter oil droplet pinch-off in this situation mainly depends on the global geometry of the blob rather than any local feature or perturbation of the blob shape. Such an observation has also been supported in previous studies for the end-pinching process of a drop under an extensional flow (Stone *et al.* 1986; Stone & Leal 1989*b*). In addition, the

strong dependence of R_d on μ_w instead of μ_o suggests that the droplet pinch-off process is mainly driven by the viscous stress generated on the water–oil interface from the bulk liquid. This observation is also consistent with previous experimental observations for droplet break-up, showing that the role of the drop viscosity is minor under an extensional flow with similar viscosity ratios as in our experiments (i.e. $0.1 < \mu_o/\mu_w < 18$) (Grace 1982).

Using dimensional analysis and the above experimental observations, we expect that the dimensionless daughter oil droplet size could be determined by multiple dimensionless groups as

$$\frac{R_d}{R} = F\left(Oh_w, \psi_o, Bo_b, \frac{\rho_o}{\rho_w}, \frac{\gamma_{oa}}{\gamma_{ow}}\right), \tag{3.1}$$

where

$$Oh_w = \frac{\mu_w}{\sqrt{\rho_w \gamma_{ow} R}}, \quad Bo_b = \frac{\rho_w g R_o^2}{\gamma_{ow}}. \tag{3.2a,b}$$

Here g is the gravitational acceleration. The effect of gravity is negligible with $Bo_b \ll 1$ (the ratio between the gravitational and capillary effects). Due to the limitation of the experimentally available liquids, ρ_o/ρ_w and γ_{oa}/γ_{ow} remain almost constant, so their variation is not considered yet in the current work. We note that, in the current range of Oh_w (ratio between inertia-capillary and visco-capillary velocities) between 0.004 and 0.04, the bubble cavity collapsing is considered as an inertia-capillary process (Gordillo & Rodríguez-Rodríguez 2019). Thus, we expect to obtain R_d/R as a function of

$$\frac{R_d}{R} = F(Oh_w, \psi_o). \tag{3.3}$$

In the following, we aim to derive the scaling law for R_d/R by considering the oil blob elongation process and the subsequent end-pinching process.

3.2. *Oil blob elongation under the extensional flow developed by cavity collapsing*

With high-speed observation, we further characterize the oil blob deformation under the extensional flow developed by bubble cavity collapsing. To track the thinning of the oil blob, we measure the maximum width of oil blob $2W$ as illustrated in figure 3(*a*,*b*). The initial oil blob width $2W_0$ is measured as the maximum horizontal dimension of the oil blob at $t = 0$, while the subsequent evolution of $2W$ is determined below the oil–air interface at $t = 0$ (figure 3*a*,*b*). We note that during the oil blob elongation, W is measured at the same horizontal location with W_0 (figure 3*a*), while after the neck of the bulbous end starts to form, W is defined as the maximum width of the bulbous end (figure 3*b*). The submerged part of the oil blob can be approximated as a semi-spheroid shape before a neck initiates (figure 3*c*). Figure 3(*d*) shows that W/W_0 first decreases and then increases with t. The initial decrease of W represents the overall thinning of the blob, while the later increase of W indicates that the width of the bulbous end exceeds that of the central portion of the blob. The regimes for the decrease and increase of W/W_0 are thus referred to as elongation and end-pinching regimes, respectively, in the later discussion.

In the elongation regime, W/W_0 initially decreases quickly because the oil blob keeps thinning as it is elongated by the extensional flow. To understand how the extensional flow affects the early thinning process of the blob, we consider the characteristic strain rate $\dot{\epsilon}$ of the flow, which was shown to be crucial for the characterization of a drop deformation in an extensional flow (Stone *et al.* 1986). Here, the elongation flow is caused by the focusing of

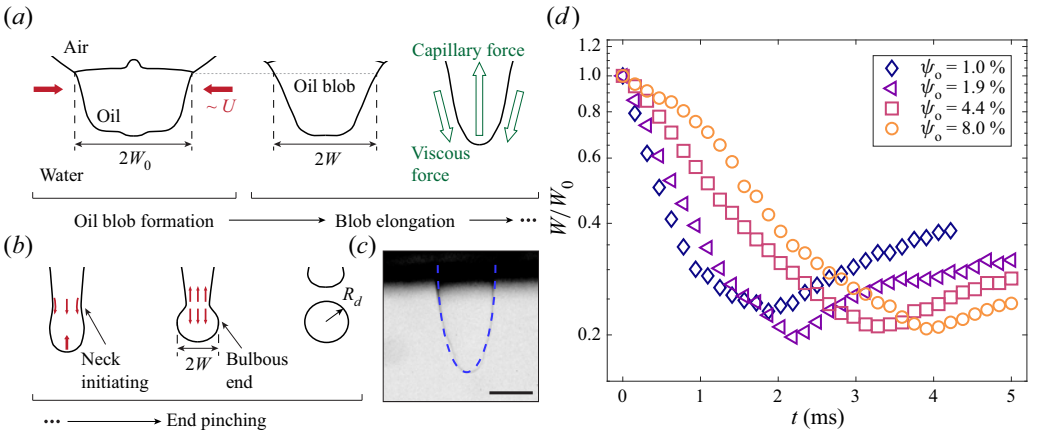

Figure 3. (*a*) Schematics of oil blob formation and elongation under an extensional flow induced by cavity collapse, starting from the moment when the upward jet is initiated. (*b*) Schematics showing the further blob evolution and end pinching following (*a*). The red arrows in (*a*) and (*b*) indicate the flow directions, and the green arrows in (*a*) sketch the forces. (*c*) The comparison between the blob shape in the experiment and a spheroid approximation (blue dashed line). The experimental image is obtained from an oil-coated bubble bursting with $\mu_w = 2.1$ mPa s, $\mu_o = 0.9$ mPa s and $\psi_o = 5.6\,\%$ at $t = 2.1$ ms. The scale bar represents 0.5 mm. (*d*) Evolution of W/W_0 with t at different ψ_o with $\mu_w = 2.1$ mPa s and $\mu_o = 0.9$ mPa s.

the capillary waves during cavity collapse, where the capillary wave propagation velocity U scales with the inertia-capillary velocity U_c as $U \sim U_c = \sqrt{\gamma/(\rho_w R)}$ (Krishnan, Hopfinger & Puthenveettil 2017; Gordillo & Rodríguez-Rodríguez 2019). For bare bubble bursting, the characteristic length scale is the bubble radius R, suggesting that the strain rate scales as $\dot{\epsilon} \sim U/R \sim \sqrt{\gamma/(\rho_w R^3)}$. This is in agreement with the scaling law for the maximum extensional strain rate in bare bubble bursting, $\dot{\epsilon}_{max} \sim \gamma^{0.46} R^{-1.68}$, numerically reported by Tran *et al.* (2016). However, in our experiments of oil-coated bubble bursting, our previous work (Yang *et al.* 2023) shows that the capillary wave propagation speed scales with $\sqrt{\gamma_e/(\rho_w R)}$, where $\gamma_e = \gamma_{ow} + \gamma_{oa}$ is the effective surface tension of the compound interface. In addition, the oil blob introduces a local length scale that sets the strain rate of the oil blob elongation. Using the characteristic length scale of effective oil blob radius R_o, we obtain the characteristic strain rate on the oil blob from the extensional flow as

$$\dot{\epsilon} \sim \frac{U}{R_o} \sim \sqrt{\frac{\gamma_e}{\rho_w R^3}}\psi_o^{-1/3}. \tag{3.4}$$

At the later stage of the elongation regime, the oil blob deformation becomes significant and the thinning slows down (figure 3*d*), which indicates that a resistant force develops and weakens the elongation rate driven by the viscous stress. The oil blob finally reaches a maximum deformation, which sets the initial condition of the subsequent end-pinching process. The characteristic Weber number in this stage, defined as the ratio between inertial and capillary effects, can be estimated as $We = \rho_w U_c^2 (2W_{min})/\gamma_{ow} = O(10^{-1})$. In addition, the local Reynolds number $Re = \rho_w U_c (2W_{min})/\mu_w$ (ratio between inertial and viscous effects) is estimated to $\leq O(10^2)$. It has been shown that, in this range of dimensionless groups with the density ratio at approximately 1, the deformation of the blob is mainly driven by the viscous stress since contributions of the dynamic pressure (inertial effect) across the interface essentially cancel each other (Ramaswamy & Leal 1997). Thus, we consider the viscous force as the dominant driving force in the blob thinning process.

We observe the curvature of the oil blob at the bottom end keeps increasing, resulting in a larger capillary pressure, $\gamma_{ow}\Delta\kappa$, where $\Delta\kappa$ is the maximum curvature variation along the oil blob interface. Therefore, the capillary pressure variation between the bottom end and the central portion of the blob tends to resist the deformation driven by the viscous stress $\mu_w\dot{\epsilon}$ induced by the extensional outer flow (Stone *et al.* 1986; Stone & Leal 1989*a*). When the thinning ceases and W approaches its minimum value W_{min} (figure 3*d*), the viscous stress and the capillary pressure are balanced as

$$\mu_w\dot{\epsilon} \sim \gamma_{ow}\Delta\kappa. \tag{3.5}$$

The submerged part of the oil blob can be approximated as a semi-spheroid shape before a neck initiates (figure 3*c*). Previous experimental studies have also reported that a drop elongated by an extensional outer flow can be estimated as a spheroidal shape before a neck forms (Stone *et al.* 1986; Li *et al.* 2000). Therefore, $\Delta\kappa$ is estimated as the curvature difference between the tip and the equator of the spheroid. Considering W_{min} as the characteristic half-width, we then estimate $\Delta\kappa \sim 2L_{max}/W_{min}^2(1 + O(W_{min}/L_{max}))$, where L_{max} is the characteristic half-length of the elongated oil blob. While we cannot directly visualize the upper part of the blob above the air–water surface to obtain L_{max}, we estimate $L_{\max}$ by considering the mass conservation of the oil blob, i.e. $W_{min}^2 L_{max} \sim V_o \sim R^3\psi_o$. This estimation is consistent in order of magnitude with the experimentally visible length of the oil blob under the interface. In our experiments, W_{min}/R_o ranges between 0.2 and 0.6, so we further obtain that $W_{min}/L_{max} \sim (W_{min}/R_o)^3 \leq O(10^{-1})$. Neglecting the higher-order terms of $O(W_{min}/L_{max})$, the characteristic curvature variation of the oil blob is eventually estimated as

$$\Delta\kappa \sim \frac{R^3\psi_o}{W_{min}^4}. \tag{3.6}$$

Combining (3.4)–(3.6), we obtain

$$\frac{W_{min}}{R} \sim \left(\frac{\mu_w}{\sqrt{\gamma_{ow}\rho_w R}}\right)^{-1/4}\left(\frac{\gamma_{ow}}{\gamma_e}\right)^{1/8}\psi_o^{1/3}, \tag{3.7}$$

which describes the oil blob width at the end of the elongation process as well as at the beginning of the end-pinching process.

3.3. *End pinching and scaling law for the daughter droplet size*

When the elongation rate of the oil blob becomes marginal and the oil blob reaches a maximum deformation, a bulbous end forms and grows in size, a typical feature previously reported for end pinching (Stone *et al.* 1986; Stone & Leal 1989*b*). This regime is associated with the increase of W/W_0 (figure 3*d*). The consequent convex region produces a local capillary pressure minimum, and the flow into the region initiates a neck above it. Next, the high capillary pressure at the neck continues to drive oil away from this neck, and therefore the neck continues to thin until pinch-off. This is referred to as the end-pinching process (figure 3*b*). We note that the entire contraction and breakup dynamics for end pinching has also been modelled by simulations (Notz & Basaran 2004; Anthony *et al.* 2019; Wang *et al.* 2019). We believe that such an end-pinching instability is the main mechanism for the daughter droplet to form at the end of the blob, given the similar experimental observations with previously reported retractive end pinching (Stone *et al.* 1986; Marks 1998; Li *et al.* 2000). Here, retractive end pinching refers to the pinch-off that develops at the end of a stretched drop retracting due to a decaying outer flow.

We experimentally observe the flow features that the oil bulb radius grows in time, similar to retractive end pinching, and that the produced daughter droplet size is directly related to the blob deformation.

In addition, such retractive end pinching is controlled by both the drop/bulk viscosity ratio and the drop elongation ratio, the latter being defined as the ratio between the maximum half-length L_{max} of the stretched drop and the initial radius of the drop (Stone *et al.* 1986; Stone & Leal 1989*a*). Considering R_o as the initial radius of the oil blob, the elongation ratio is estimated as $L_{max}/R_o \sim (W_{min}/R_o)^{-2}$ from mass conservation, which is found to be ≥ 3 in our experiments. It has been suggested that the smallest critical elongation ratio that produces retractive end pinching is ≈ 3.4 regarding the viscosity ratio range in our study (Stone *et al.* 1986). Thus, the retractive end pinching could be reasonably initiated in the elongated blob at the bubble cavity bottom. We note that the extensional flow produced by cavity collapse is not stopped abruptly when the oil blob deforms, which also facilitates end pinching, as suggested by Stone & Leal (1989*a*). Furthermore, the Ohnesorge number for the oil blob at breakup, $Oh_{ob} = \mu_o/\sqrt{\rho_o \gamma_{ow} W_{min}}$, is estimated to be $O(0.01)$. This is consistent with the value expected in the end-pinching regime for filament breakup in air (Notz & Basaran 2004; Anthony *et al.* 2019).

Now we derive the scaling law for the entrained daughter oil droplets from end pinching. It has been shown that, for end pinching from a slender cylinder, the radius of the daughter droplet is proportional to the radius of the slender cylinder (Schulkes 1996; Wang & Bourouiba 2018). Thus, we obtain $R_d \sim W_{min}$, which can be rationalized as follows. The daughter droplet size from end pinching is directly related to the growth rate of the bulbous end and the time for pinch-off. For $Oh_{ob} = O(0.01)$, as in our case, the tip retraction velocity scales as $U_{tip} \sim \sqrt{\gamma_{ow}/(\rho_o W_{min})}$ (Anthony *et al.* 2019). Meanwhile, the breakup time scale depends on the inertia-capillary dynamics and scales as $t_{cap} \sim \sqrt{\rho_o W_{min}^3/\gamma_{ow}}$ (Gordillo & Gekle 2010; Anthony *et al.* 2019). Therefore, the retraction length of the tip for the daughter droplet before breakup is estimated to be $L_c \sim U_{tip} t_{cap} \sim W_{min}$. Using volume conservation, we confirm that $R_d \sim (W_{min}^2 L_c)^{1/3} \sim W_{min}$. Indeed, figure 4(*a*) shows that $R_d/W_{min} = 1.4 \pm 0.3$, consistent with the value of ≈ 1.5 for the end-pinching dynamics reported by Gordillo & Gekle (2010) and Wang & Bourouiba (2018). Therefore, the dimensionless daughter oil drop radius follows

$$\frac{R_d}{R} \sim \frac{W_{min}}{R} \sim \left(\frac{\mu_w}{\sqrt{\gamma_{ow}\rho_w R}}\right)^{-1/4} \left(\frac{\gamma_{ow}}{\gamma_e}\right)^{1/8} \psi_o^{1/3}. \tag{3.8}$$

Noting that $(\gamma_{ow}/\gamma_e)^{1/8} \approx 1$ in our experiments (table 1), (3.8) reduces to

$$\frac{R_d}{R} \sim Oh_w^{-1/4} \psi_o^{1/3}. \tag{3.9}$$

Figure 4(*b*) shows a reasonably good collapse (with a coefficient of determination $R^2 = 0.89$) of the scaled daughter droplet radius in all our experiments onto the master curve described by (3.9), over a wide range of Oh_w ($\approx$0.004–0.04) and ψ_o ($\approx$0.1 %–10 %). The comparison indicates that our scaling law captures well the physical feature of daughter oil droplet formation. Our model suggests that the daughter droplet radius is related to the blob size determined by the global geometry during end pinching. In addition, with the increase of Oh_w, the viscous stress from the bulk aqueous solution becomes stronger than the resisting capillary pressure, which results in a stronger deformation of the oil blob and a smaller daughter oil droplet.

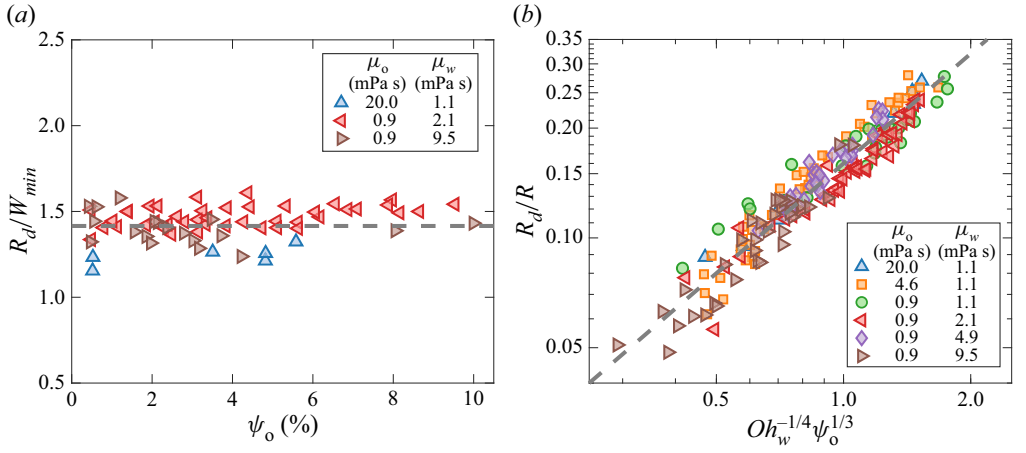

Figure 4. (*a*) The ratio between the daughter oil droplet radius and the minimum half-width of the blob, R_d/W_{min}, as a function of ψ_o, regarding the largest, intermediate and smallest oil-to-water viscosity ratio in the experiments. The dashed line represents the average value of $R_d/W_{min} = 1.4$. (*b*) Collapsing of the experimentally measured daughter oil droplet radius on the master curve $R_d/R = 0.16Oh_w^{-1/4}\psi_o^{1/3}$, as shown by the grey dashed line.

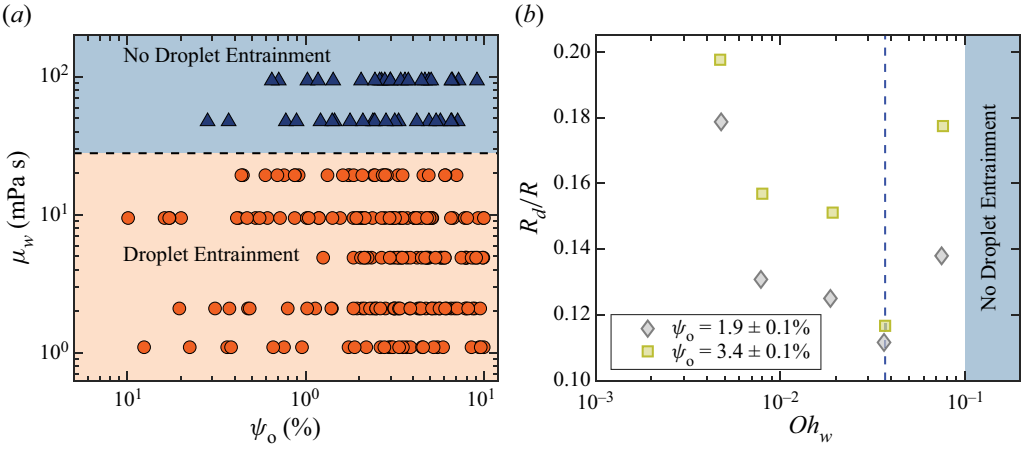

Figure 5. (*a*) Phase diagram of daughter oil droplet entrainment at different ψ_o and μ_w with $\mu_o = 0.9$ mPa s. Cases with daughter droplet and no daughter droplet are indicated by orange circles and blue triangles, respectively. (*b*) Dimensionless daughter oil droplet radius R_d/R, as a function of Oh_w at selected ψ_o, with $\mu_o = 0.9$ mPa s. The dashed line indicates a critical Ohnesorge number $Oh_c = 0.037$. The shaded region represents the regime where no daughter oil droplet is entrained.

3.4. *Discussion for high viscosity regime*

In this section, we will briefly discuss some distinct features of the daughter droplet entrainment by oil-coated bubble bursting in the high viscosity regime, regarding the limitation of our scaling analysis. We note that our current study focuses on the inertia-capillary collapse of the bubble cavity given the low bulk Ohnesorge number of $Oh_w \leq 0.037$. With a further increase of the viscosity of the aqueous solution μ_w and thus Oh_w, we observe no oil droplet entrainment when $\mu_w \geq 50$ mPa s, with $\mu_o = 0.9$ mPa s and ψ_o between 0.1 % and 10 % (figure 5*a*). Specifically, R_d/R increases with μ_w when

$Oh_w \approx 0.037$–0.1 at a fixed ψ_o, and there is no droplet entrainment when $Oh_w > 0.1$ (figure 5*b*). We denote this regime of $Oh_w > 0.037$ as the high viscosity regime, in which the daughter droplet size shows an opposite trend compared with the cases with smaller Oh_w in the inertia-capillary regime. We note that the non-monotonic transition occurs at $Oh_w \approx 0.037$. In fact, a similar non-monotonic dependence of the upward jet size on the Ohnesorge number of the bulk liquid has also been observed in the context of bare bubble bursting. The critical Ohnesorge number at transition is determined to be $\approx$0.03–0.04 by experiments and simulations (Brasz *et al.* 2018; Deike *et al.* 2018; Gordillo & Rodríguez-Rodríguez 2019), similar to our observation in figure 5(*b*). Following the flow characterization by bubble bursting, at a similar high viscosity regime, it has been shown that the strain rate in the bulk extensional flow will be limited by the strong viscous effect (Gañán-Calvo & López-Herrera 2021), leading to a deviation from (3.4). Hence, the decrease in viscous stress with an increasing Oh_w results in an increasing daughter droplet size. Ultimately, the extensional flow will be significantly weakened, resulting in insufficient viscous stress to elongate the oil blob and thus no daughter oil droplets. Although the daughter oil droplet size increases in a relatively narrow range of Oh_w, we believe that further studies in this high viscosity regime might provide more mechanistic insights into the dynamics of compound bubble bursting.

4. Concluding remarks

In this paper, we investigate the daughter oil droplet entrainment during oil-coated bubble bursting. The oil coating around the bubble surface is swept downward by the capillary wave focusing during cavity collapse, forming an oil blob at the cavity nadir. This oil blob first elongates vertically under the extensional flow induced by the capillary wave focusing during bubble cavity collapse, then undergoes an end-pinching process that tears the daughter oil droplets off from the blob end. We find that the daughter droplet size increases with the oil coating volume fraction ψ_o and decreases with the Ohnesorge number of the bulk liquid Oh_w. We highlight that the daughter oil droplet size is set by the maximum deformation of the elongated oil blob under the extensional flow, which is determined by the visco-capillary balance at the late stage of oil blob elongation. Furthermore, our scaling law based on ψ_o and Oh_w well describes the daughter droplet size measured experimentally for Oh_w between 0.004 and 0.04. In addition, when Oh_w is further increased, the daughter oil droplet increases in size and eventually vanishes because of stronger viscous effects. A detailed characterization of the flow field in the oil and the bulk liquid with particle image velocimetry will help better characterize the effect of viscous stresses leading to end pinching, which could be carried out in future work. Our results not only advance the fundamental understanding of multiphase flow physics related to free-surface bubbles, but might also shed light on the transport and fate of oil and other bulk contaminants in natural water bodies. Furthermore, our experimental study can serve as a benchmark for future simulation studies of the oil-coated bubble bursting.

Although in the current work we only focus on the formation of the largest daughter droplet, other flow physics may need to be further considered to fully describe multiple smaller oil droplets formed during the pinch-off of the oil blob. Such smaller droplets may be induced by Rayleigh–Plateau instability (Stone & Leal 1989*b*) or capillary wave breakup (Anthony *et al.* 2019), which is beyond the scope of this study. In addition, surfactant, either as an additive or a contaminant, presents in a multitude of natural and industrial set-ups, such as contaminated water bodies and inkjet printing. When surfactants are included in the experimental system, we observe a significant increase of the daughter droplet size compared with the surfactant-free case in our preliminary experiments.

In addition to reducing the surface tension, the non-uniform distribution of surfactants at the interface under the fluid motion has been shown to produce an extra Marangoni stress, allowing flows into the bulbous end during the neck evolution and opposing the end pinching, thus promoting larger droplet formation (Constante-Amores *et al.* 2020; Kamat *et al.* 2020). More systematic experiments on the effects of surfactant will be conducted in the near future.

In addition, previous studies show that the hydrodynamic stresses produced during bubble bursting can damage living organisms (Chalmers & Bavarian 1991; Boulton-Stone & Blake 1993; Walls *et al.* 2017), while our study also exemplifies that the hydrodynamic stresses produced in oil-coated, contaminated bubble bursting can effectively tear the oil coating into droplets as small as $\sim 100\,\mu$m. This dispersal dynamics may facilitate biodegradation because of the high surface-to-volume ratio and long residence time of the droplets (Feng *et al.* 2014; Socolofsky *et al.* 2019). We note that our current study concerns bubbles coated with a Newtonian fluid layer. Considering the physicochemically complex contaminants in nature and engineering, further investigation for bubbles coated with non-Newtonian complex fluids would also be of interest.

Declaration of interests. The authors report no conflict of interest.

Author ORCIDs.
Zhengyu Yang https://orcid.org/0000-0002-7865-240X;
Bingqiang Ji https://orcid.org/0000-0002-4873-7090;
Jie Feng https://orcid.org/0000-0002-4891-9214.

References

Anthony, C.R., Kamat, P.M., Harris, M.T. & Basaran, O.A. 2019 Dynamics of contracting filaments. *Phys. Rev. Fluids* **4** (9), 093601.

Behrens, S.H. 2020 Oil-coated bubbles in particle suspensions, capillary foams, and related opportunities in colloidal multiphase systems. *Curr. Opin. Colloid Interface Sci.* **50**, 101384.

Boulton-Stone, J.M. & Blake, J.R. 1993 Gas bubbles bursting at a free surface. *J. Fluid Mech.* **254**, 437–466.

Brasz, C.F., Bartlett, C.T., Walls, P.L.L., Flynn, E.G., Yu, Y.E. & Bird, J.C. 2018 Minimum size for the top jet drop from a bursting bubble. *Phys. Rev. Fluids* **3** (7), 074001.

Chalmers, J.J. & Bavarian, F. 1991 Microscopic visualization of insect cell-bubble interactions. 2. The bubble film and bubble rupture. *Biotechnol. Progr.* **7** (2), 151–158.

Constante-Amores, C.R., Kahouadji, L., Batchvarov, A., Shin, S., Chergui, J., Juric, D. & Matar, O.K. 2020 Dynamics of retracting surfactant-laden ligaments at intermediate Ohnesorge number. *Phys. Rev. Fluids* **5** (8), 084007.

Deike, L. 2022 Mass transfer at the ocean–atmosphere interface: the role of wave breaking, droplets, and bubbles. *Annu. Rev. Fluid Mech.* **54**, 191–224.

Deike, L., Ghabache, E., Liger-Belair, G., Das, A.K., Zaleski, S., Popinet, S. & Séon, T. 2018 Dynamics of jets produced by bursting bubbles. *Phys. Rev. Fluids* **3** (1), 013603.

Duchemin, L., Popinet, S., Josserand, C. & Zaleski, S. 2002 Jet formation in bubbles bursting at a free surface. *Phys. Fluids* **14** (9), 3000–3008.

Feng, J., Roché, M., Vigolo, D., Arnaudov, L.N., Stoyanov, S.D., Gurkov, T.D., Tsutsumanova, G.G. & Stone, H.A. 2014 Nanoemulsions obtained via bubble-bursting at a compound interface. *Nat. Phys.* **10** (8), 606–612.

Gañán-Calvo, A.M. & López-Herrera, J.M. 2021 On the physics of transient ejection from bubble bursting. *J. Fluid Mech.* **929**, A12.

Garcia-Briones, M.A., Brodkey, R.S. & Chalmers, J.J. 1994 Computer simulations of the rupture of a gas bubble at a gas–liquid interface and its implications in animal cell damage. *Chem. Engng Sci.* **49** (14), 2301–2320.

Garcia-Briones, M.A. & Chalmers, J.J. 1994 Flow parameters associated with hydrodynamic cell injury. *Biotechnol. Bioengng* **44** (9), 1089–1098.

GORDILLO, J.M. & GEKLE, S. 2010 Generation and breakup of worthington jets after cavity collapse. Part 2. Tip breakup of stretched jets. *J. Fluid Mech.* **663**, 331–346.

GORDILLO, J.M. & RODRÍGUEZ-RODRÍGUEZ, J. 2019 Capillary waves control the ejection of bubble bursting jets. *J. Fluid Mech.* **867**, 556–571.

GRACE, H.P. 1982 Dispersion phenomena in high viscosity immiscible fluid systems and application of static mixers as dispersion devices in such systems. *Chem. Engng Commun.* **14** (3–6), 225–277.

HARIADI, R.F., WINFREE, E. & YURKE, B. 2015 Determining hydrodynamic forces in bursting bubbles using DNA nanotube mechanics. *Proc. Natl Acad. Sci. USA* **112** (45), E6086–E6095.

JI, B., SINGH, A. & FENG, J. 2021*a* Oil column pinch-off controls the oil fraction of the oil-coated bubble. *Phys. Fluids* **33** (10), 103316.

JI, B., YANG, Z. & FENG, J. 2021*b* Compound jetting from bubble bursting at an air-oil-water interface. *Nat. Commun.* **12** (1), 1–10.

JI, B., YANG, Z. & FENG, J. 2021*c* Oil-coated bubble formation from submerged coaxial orifices. *Phys. Rev. Fluids* **6** (3), 033602.

JOHANSEN, C., TODD, A.C. & MACDONALD, I.R. 2017 Time series video analysis of bubble release processes at natural hydrocarbon seeps in the Northern Gulf of Mexico. *Mar. Petrol. Geol.* **82**, 21–34.

KAMAT, P.M., WAGONER, B.W., CASTREJÓN-PITA, A.A., CASTREJÓN-PITA, J.R., ANTHONY, C.R. & BASARAN, O.A. 2020 Surfactant-driven escape from endpinching during contraction of nearly inviscid filaments. *J. Fluid Mech.* **899**, A28.

KRISHNAN, S., HOPFINGER, E.J. & PUTHENVEETTIL, B.A. 2017 On the scaling of jetting from bubble collapse at a liquid surface. *J. Fluid Mech.* **822**, 791–812.

LHUISSIER, H. & VILLERMAUX, E. 2012 Bursting bubble aerosols. *J. Fluid Mech.* **696**, 5–44.

LI, J., RENARDY, Y.Y. & RENARDY, M. 2000 Numerical simulation of breakup of a viscous drop in simple shear flow through a volume-of-fluid method. *Phys. Fluids* **12** (2), 269–282.

MACINTYRE, F. 1972 Flow patterns in breaking bubbles. *J. Geophys. Res.* **77** (27), 5211–5228.

MARKS, C.R. 1998 Drop breakup and deformation in sudden onset strong flows. PhD thesis, University of Maryland, College Park, MD.

NOTZ, P.K. & BASARAN, O.A. 2004 Dynamics and breakup of a contracting liquid filament. *J. Fluid Mech.* **512**, 223–256.

POULAIN, S. & BOUROUIBA, L. 2018 Biosurfactants change the thinning of contaminated bubbles at bacteria-laden water interfaces. *Phys. Rev. Lett.* **121** (20), 204502.

RAMASWAMY, S. & LEAL, L.G. 1997 A note on inertial effects in the deformation of Newtonian drops in a uniaxial extensional flow. *Intl J. Multiphase Flow* **23** (3), 561–574.

SCHULKES, R.M.S.M. 1996 The contraction of liquid filaments. *J. Fluid Mech.* **309**, 277–300.

SOCOLOFSKY, S.A., GROS, J., NORTH, E., BOUFADEL, M.C., PARKERTON, T.F. & ADAMS, E.E. 2019 The treatment of biodegradation in models of sub-surface oil spills: a review and sensitivity study. *Mar. Pollut. Bull.* **143**, 204–219.

SONG, B. & SPRINGER, J. 1996 Determination of interfacial tension from the profile of a pendant drop using computer-aided image processing. 2. Experimental. *J. Colloid Interface Sci.* **184** (1), 77–91.

STONE, H.A., BENTLEY, B.J. & LEAL, L.G. 1986 An experimental study of transient effects in the breakup of viscous drops. *J. Fluid Mech.* **173**, 131–158.

STONE, H.A. & LEAL, L.G. 1989*a* The influence of initial deformation on drop breakup in subcritical time-dependent flows at low Reynolds numbers. *J. Fluid Mech.* **206**, 223–263.

STONE, H.A. & LEAL, L.G. 1989*b* Relaxation and breakup of an initially extended drop in an otherwise quiescent fluid. *J. Fluid Mech.* **198**, 399–427.

SU, L., XU, Z. & MASLIYAH, J. 2006 Role of oily bubbles in enhancing bitumen flotation. *Miner. Engng* **19** (6–8), 641–650.

TRAN, T.T., LEE, E.G., LEE, I.S., WOO, N.S., HAN, S.M., KIM, Y.J. & HWANG, W.R. 2016 Hydrodynamic extensional stress during the bubble bursting process for bioreactor system design. *Korea-Aust. Rheol. J.* **28**, 315–326.

TSENG, R.-S., VIECHNICKI, J.T., SKOP, R.A. & BROWN, J.W. 1992 Sea-to-air transfer of surface-active organic compounds by bursting bubbles. *J. Geophys. Res.* **97** (C4), 5201–5206.

VISSER, C.W., AMATO, D.N., MUELLER, J. & LEWIS, J.A. 2019 Architected polymer foams via direct bubble writing. *Adv. Mater.* **31** (46), 1904668.

WALLS, P.L.L., BIRD, J.C. & BOUROUIBA, L. 2014 Moving with bubbles: a review of the interactions between bubbles and the microorganisms that surround them. *Am. Zool.* **54** (6), 1014–1025.

WALLS, P.L.L., MCRAE, O., NATARAJAN, V., JOHNSON, C., ANTONIOU, C. & BIRD, J.C. 2017 Quantifying the potential for bursting bubbles to damage suspended cells. *Sci. Rep.* **7** (1), 15102.

WANG, F., CONTÒ, F.P., NAZ, N., CASTREJÓN-PITA, J.R., CASTREJÓN-PITA, A.A., BAILEY, C.G., WANG, W., FENG, J.J. & SUI, Y. 2019 A fate-alternating transitional regime in contracting liquid filaments. *J. Fluid Mech.* **860**, 640–653.

WANG, X., *et al.* 2017 The role of jet and film drops in controlling the mixing state of submicron sea spray aerosol particles. *Proc. Natl Acad. Sci. USA* **114** (27), 6978–6983.

WANG, Y. & BOUROUIBA, L. 2018 Unsteady sheet fragmentation: droplet sizes and speeds. *J. Fluid Mech.* **848**, 946–967.

WILSON, T.W., *et al.* 2015 A marine biogenic source of atmospheric ice-nucleating particles. *Nature* **525** (7568), 234–238.

YANG, Z., JI, B., AULT, J.T. & FENG, J. 2023 Enhanced singular jet formation in oil-coated bubble bursting. *Nat. Phys.* **19**, 884–890.

ZHOU, F., WANG, L., XU, Z., LIU, Q., DENG, M. & CHI, R. 2014 Application of reactive oily bubbles to bastnaesite flotation. *Miner. Engng* **64**, 139–145.